A novel epitaxially grown LSO-based thin film scintillator for micro-imaging using hard synchrotron radiation

Paul-Antoine Douissard,[a]* Angelica Cecilia,[b] Thierry Martin,[a] Valentin Chevalier,[a] Maurice Couchaud,[c] Tilo Baumbach,[b] Klaus Dupré,[d] Markus Kühbacher[e] and Alexander Rack[a,b]

[a]*European Synchrotron Radiation Facility, F-38043 Grenoble Cedex, France,* [b]*Karlsruhe Institute of Technology – ANKA, D-76021 Karlsruhe, Germany,* [c]*CEA/LETI, F-38054 Grenoble Cedex, France,* [d]*FEE GmbH, D-55743 Idar-Oberstein, Germany, and* [e]*Helmholtz-Zentrum Berlin für Materialien und Energie, D-14109 Berlin, Germany. E-mail: paul_antoine.douissard@esrf.fr*

(Received 0 XXXXXXX 0000; accepted 0 XXXXXXX 0000)

LSO:Tb; luminescence; synchrotron instrumentation; scintillator; X-ray phase contrast; microtomography; spatial resolution; detective quantum efficiency; X-ray detection; radiography; X-rays; synchrotron radiation

Abstract

The efficiency of high resolution pixel detectors for hard X-rays is nowadays one of the major criteria which drives the feasibility of imaging experiments and in general the performance of an experimental station for synchrotron-based microtomography and radiography. We focus on the luminescent screen used for the indirect detection in order to increase the detective quantum efficiency: a novel scintillator based on doped Lu_2SiO_5 (LSO), epitaxially grown as thin film via the Liquid Phase Epitaxy (LPE) technique. We show that by using adapted growth and doping parameters as

well as a dedicated substrate, the scintillation behaviour of a LSO-based thin crystal together with the material high stopping power allows for high-performance indirect X-ray detection. In detail, the conversion efficiency, the radioluminescence spectra, the optical absorption spectra under UV/visible light and the afterglow are investigated. A setup to study the effect of the thin film scintillator's temperature on its conversion efficiency is described as well. It delivers knowledge which is important when working with higher photon flux densities and the corresponding high heat load on the material. Additionally, X-ray imaging systems based on different diffraction limited visible light optics and CCD cameras using among others LSO-based thin film are compared. Finally, the performance of the LSO thin film is illustrated by imaging a honey bee leg, demonstrating the value of efficient high-resolution Computed Tomography (CT) for life sciences.

1. Introduction

During the 1980s, one of the major questions to be answered for synchrotron-based micro-imaging was which kind of detector system would reach for high spatial resolutions below submicrometer, see, e. g., (Spiller, 1980), (Flannery *et al.*, 1987), (Spanne & Rivers, 1987), (Kinney *et al.*, 1989), (Bonse *et al.*, 1989), (Graeff & Engelke, 1991). During the 1990s it became clear that indirect pixel detectors provided the optimum solution. Here, the luminescence image of a scintillator screen is coupled to a digital camera via diffraction limited visible light optics (Hartmann *et al.*, 1975). This approach allowed for building robust and efficient detectors consisting of components which were already commercially available, see, e. g., (Koch, 1994), (Bonse & Busch, 1996), (Lee *et al.*, 1997). By the end of that decade spatial resolutions below submicrometer were established as standard technique by introducing thin single-crystal film scintillators (SCF) for the indirect detection (Koch *et al.*, 1998), (Koch

et al., 1999*b*). Using these high resolution indirect pixel detectors allowed for numerous applications in diverse fields such as life science, materials research or archaeology (for a detailed review see, e. g., S. R. Stock (Stock, 1999), (Stock, 2008), J. Baruchel et al. (Baruchel *et al.*, 2002), (Baruchel *et al.*, 2006) or J. Banhart et al. (Banhart, 2008)). Furthermore, novel contrast schemes like X-ray inline phase contrast, rocking curve imaging, topo-tomography, diffraction enhanced imaging or holotomography could be exploited (Cloetens *et al.*, 1996), (Snigirev *et al.*, 1995), (Nugent *et al.*, 1996), (Cloetens *et al.*, 1999), (Ludwig *et al.*, 2001), (Lübbert *et al.*, 2000), (Chapman *et al.*, 1997). High resolution micro-imaging stations are operating nowadays at many synchrotron light sources in the world (Stampanoni *et al.*, 2007), (Wang *et al.*, 2001), (Weitkamp *et al.*, 1999), (Uesugi *et al.*, 2004), (Beckmann *et al.*, 2004), (Rack *et al.*, 2008), (Di Michiel *et al.*, 2005), (Rack *et al.*, 2009*b*). This development is well documented in the SPIE conference series "Developments in X-ray Tomography I-VII" and the corresponding proceedings.

Recently, the spatial resolution has reached the nanometer range by combining indirect X-ray detectors with different X-ray optics (Ortega *et al.*, 2007), (Bleuet *et al.*, 2009), (Schroer *et al.*, 2002), (Modregger *et al.*, 2007), (Stampanoni *et al.*, 2005), (Reznikova *et al.*, 2007), (Rack *et al.*, 2008), (Feser *et al.*, 2008). Here, as the higher resolutions are reached by the X-ray optics, the demand for scintillator screens with higher efficiency is increasing in order to make optimal use of the available photon flux density or to reduce the dose to the samples. Higher efficiency is also required when using indirect detectors for synchrotron-based high-speed imaging (Di Michiel *et al.*, 2005), (Wang *et al.*, 2008), (Rack *et al.*, 2009*a*).

Our approach to increase the detective quantum efficiency (DQE) of high resolution indirect pixel detectors is the use of optimized luminescent screens. A dense scintillator material, available as thin film with high optical quality, high stopping power and an

emission spectrum matching the sensitivity of the camera used can increase the overall DQE by up to one order of magnitude compared to commercially available systems (Koch *et al.*, 1998), (Koch *et al.*, 1999*b*), (Martin & Koch, 2006).

Within a project of the Sixth Framework Programme (FP6) of the European Commission (Scin^{TAX} – STRP 033 427) we developed such a new thin film scintillator for high resolution X-ray imaging (Martin *et al.*, 2009), (Dupré *et al.*, submitted 2007, published 20th and 22th May 2009), (www.scintax.eu, last visit 2010), (Cecilia *et al.*, 2010). Here, our research is based on Lu_2SiO_5 (LSO) layers grown on adapted substrates. Because of their high effective Z number, these scintillators improve significantly the efficiency of X-ray imaging detectors currently used in synchrotron facilities. The bulk scintillator material also presents interesting features for nondestructive testing applications. The major improvement obtained by using a thin LSO-based scintillator is the higher X-ray absorption compared to commonly used thin film scintillators, such as Ce-doped $Y_3Al_5O_{12}$ (YAG:Ce), Eu-doped $Lu_3Al_5O_{12}$ (LAG:Eu) or Eu-doped $Gd_3Ga_5O_{12}$ (GGG:Eu) (Martin *et al.*, 2005), (Martin & Koch, 2006), (Koch *et al.*, 1999*a*). Another advantage is that the specific substrate developed in the framework of the Scin^{TAX} project presents no parasitic luminescence under X-ray excitation (Cecilia *et al.*, 2009). This is rarely the case for substrates used today for scintillators in synchrotron X-ray imaging (Martin & Koch, 2006). Finally, the light emission of the LSO active layer was optimized by varying the dopant material and its concentration. The results are a high light yield (comparable to that of bulk YAG:Ce) as well as an emission wavelength adapted to match the quantum efficiencies of most CCD cameras.

LSO-based thin scintillator layers doped with different lanthanide ions were grown using Liquid Phase Epitaxy (LPE) (Martin *et al.*, 2009) at the French Atomic Energy Commission (CEA). Their scintillating characteristics were then studied at the Euro-

pean Synchrotron Radiation Facility (ESRF) and at the Ångströmquelle Karlsruhe (ANKA): conversion efficiency, afterglow, UV/visible light absorption and emission (measurements on the X-ray absorption efficiency have already been published in (Martin *et al.*, 2009)). In this article special emphasis is given to temperature effects on the conversion efficiency, as these can be detrimental with increasing X-ray photon flux and the corresponding heat load, i. e. when using white beam synchrotron radiation. The developed LSO thin film scintillators were also combined with different detection systems (CCD sensors and high resolution optics). The efficiency of these systems was evaluated as a function of the X-ray energy and compared to the same systems using a GGG:Eu thin film scintillator. Finally, an example of LSO application is provided consisting of an X-ray microtomography of a fine structured biological sample.

2. Hard X-ray Micro-Imaging

The first indirect detection systems were introduced in the middle of the 1970s for live topography (Hartmann *et al.*, 1975). The concept is based on combining scintillator screens with diffraction limited visible light objectives, see Fig. 1. The scintillator converts the X-ray image into a visible light image that is magnified through an objective onto a camera (nowadays commonly with a CCD- or CMOS-based sensor). A specific object plane within the scintillator is focused via the optics onto the sensor of the camera, cf., e. g., (Bonse & Busch, 1996), (Koch *et al.*, 1998), (Graafsma & Martin, 2008).

The camera type to be chosen depends on the application. Synchrotron-based microtomography typically requires high dynamic range CCDs with moderate read-out speed of several frames per second (a CCD camera explicitly developed for synchrotron-based applications is the FReLoN (Labiche *et al.*, 2007)). For fast imaging using white

synchrotron radiation, frame transfer CCDs or CMOS cameras offer much higher read-out speed but commonly with a reduced dynamic range (Di Michiel *et al.*, 2005), (Rack *et al.*, 2009*a*), (García-Moreno *et al.*, 2008).

2.1. The quest for the ideal thin film scintillator

The ideal inorganic thin film scintillator (Derenzo *et al.*, 2003), (Weber, 2002), (Koch *et al.*, 1998) to be used for micro-imaging applications should combine the following properties:

- high density, high effective Z-number,
- high light output,
- low afterglow,
- high optical quality,
- non-toxic, chemically stable under ambient conditions and easy to machine,
- emission spectrum well suited to visible light detectors,
- layer thickness $< 20\,\mu$m,
- adaptable for the LPE growth technique.

Table 1 lists Single Crystal Film (SCF) scintillating materials frequently used at the ESRF. Initially, YAG:Ce was applied as it was widely commercially available. In order to improve the stopping power, especially below the Yttrium edge of 17 keV, LAG-based crystals grown by LPE were developed in collaboration between the ESRF and the CEA (Koch *et al.*, 1999*b*). Next, GGG:Eu was introduced, showing a slightly better stopping power than LAG-based crystals, a higher light yield and a lower afterglow (Martin *et al.*, 2005).

Seen in this chronological manner, a detailed study of LSO-based SCFs is the consequent next step, as suggested by Koch et al. (Koch *et al.*, 1998). It allows one to further improve light yield, stopping power and optical match of the emission spec-

trum with the CCD quantum efficiency. Furthermore, the development of LSO-based SCFs in the framework of a FP6 program allows for transferring the technology to an industrial partner, hence making the material available for a broader community (www.scintax.eu, last visit 2010).

2.2. Spatial resolution

According to the theorem of Abbe, the maximum resolution R achievable with an indirect X-ray pixel detector is determined by the numerical aperture (NA) of the front objective and the scintillator's wavelength of maximum emission. The diffraction limit is given by the relationship (Rayleigh criterion (Born & Wolf, 1999)):

$$R = 0.66 \times \lambda/\mathrm{NA} \quad . \tag{1}$$

The effective pixel size of the camera sensor has also to be adapted to the sought resolution (Shannon's sampling theorem (Shannon & Weaver, 1963)).

The NA drives the spatial resolution of the detector and determines the depth of focus (Born & Wolf, 1999). For an indirect detector the luminescence screen has to be as thick as the depth of focus to maximise the efficiency without deteriorating the resolution. Degradation of the image can occur due to diffraction and spherical aberrations arising from the total thickness of the screen. Parallax by misalignment, i. e. an angle between X-rays and optical axis, may also degrade the image quality. Investigations on the achievable resolution by means of numerical simulations can be found in the literature (Koch *et al.*, 1998), (Stampanoni *et al.*, 2002).

The screen's substrate may also degrade the resolution, through undesired intrinsic scintillation components. As an example, the intrinsic scintillation of an undoped YAG substrate can reach in the worst case up to 20% of the total scintillation yield (Martin & Koch, 2006). When thin layers of YAG:Ce or LAG:Eu (e. g., 5 μm) deposited onto this substrate are used at high X-ray energies ($>$ 20 keV), the luminescence of the YAG

substrate becomes significant (e. g., at 15 keV, only 25% of incident X-ray photons are absorbed by a 5 μm-thick LAG:Eu screen). LAG:Eu and YAG:Ce layers grown by LPE on undoped YAG substrates are therefore not an ideal solution for high spatial resolution imaging at these energies, unless specific techniques are used to block the parasitic light (e. g., glass filters placed in the optical beam path of the detector).

The spatial resolution is also degraded by other X-ray interactions taking place in the screen: elastic scattering (Rayleigh), inelastic scattering (Compton) and photo-electric absorption. The contribution of these processes were studied in detail by T. Martin and A. Koch for LAG, YAG and GGG scintillators (Martin & Koch, 2006).

3. LSO-based thin film scintillator

LSO thin films were produced by the Liquid Phase Epitaxy (LPE) technique (Ferrand *et al.*, 1999) at the CEA-Leti (Grenoble, France). The solute materials (Lu_2O_3, SiO_2) were dissolved in a PbO/B_2O_3 solvent at high temperatures (>1000^{o}C). The dopants were chosen among the lanthanide ions and therefore the oxide forms of these dopants were added in the melt in concentrations varying between 1% and 20% atomic weight (Martin *et al.*, 2009). The atomic weight ratio of SiO_2/Lu_2O_3 was chosen so as to crystallise the LSO phase in the range of temperatures considered here. For each dopant concentration, the conversion efficiency of the layers was measured. The dopant concentration was determined in order to optimise the conversion efficiency and keep a good lattice match between the substrate and the epitaxial layer. After growth, the conversion efficiency of the epitaxial layer could be further enhanced by 20-30% by thermal annealing of the layers at 1100^{o}C during 30 h in air.

The largest area obtainable for a LSO:Tb crystal is limited by the dimensions of the crucible used for LPE. For example, at the ESRF wafers of 1" diameter (25.4 mm) can be employed as substrate. Thickness inhomo-

geneities at the edge of the substrate where the wafer is fixed during LPE prevent exploiting the full area of the crystal. Hence, commonly four active areas of approximately 8 mm × 8 mm can be obtained from a 1" wafer. The corresponding optical quality and uniformity of the crystal's surface has reached a level of perfection so that it has basically no or only negligible influence on the imaging performance of the detector. In fact, currently indirect detectors using scintillating single crystals are more affected by external impurities like dust particles sticking on the surface of the crystal, which leads to bright spots in the images.

3.1. Conversion efficiency

The conversion efficiency $\eta_{x/v}$ describes the ability of the scintillator material to convert X-rays into UV/visible light photons. In our case it is measured in the laboratory with a copper anode X-ray tube run at 20 kV and 45 mA. A 25 μm Cu X-ray absorption filter was used to select the monochromatic 8 keV emission line of the copper anode.

An X-ray imaging system based on a PCO SVGA Sensicam CCD camera and microscope optics (4x objective, 0.16 NA, 2x eyepiece) was used to acquire images of the luminescence screen. The average value $\overline{\mathrm{ADU}}$ of the flat-field (dark corrected) image intensity values (ADU) were calculated. This average value was corrected for both the absorption A(8 keV) of the layer and the CCD quantum efficiency (QE):

$$\eta_{x/v} = \frac{\overline{\mathrm{ADU}}}{\mathrm{QE} \times A(8keV)} \quad . \tag{2}$$

The above value was normalised with respect to the conversion efficiency of a bulk YAG:Ce sample used as a reference (the light output of the YAG:Ce was taken to be 35 ph/keV as specified by the supplier (www.crytur.cz, last visit 2010)).

Several dopants were investigated. From the lanthanide ions, only Eu and Tb could

be used successfully to grow thin films of good optical quality. The Ce dopant was rejected because it did not provide a good lattice match; the Tm and Sm ions were rejected due to the low conversion efficiency of the resulting layers. Table 2 shows the effect of the dopant(-combination) on the conversion efficiency after the films were optimised (with respect to growth parameters) and thermally annealed. Tb was found to be the most efficient dopant for the LSO lattice grown as a thin film (for the concentrations allowing for a good lattice match between the substrate and the layer (Martin *et al.*, 2009)). **In this case, the absolute efficiency of the scintillator can raise up to 45 ph/keV.** Codopants such as Gd, Ge and Ce were found to further improve the conversion efficiency of LSO:Tb thin films. **The maximum conversion efficiency measured for a LSO:Tb,Ce sample was 52 ph/keV.**

Our investigations showed that the conversion efficiency of Tb-doped LSO thin crystal films can rise by several percent after long exposures to X-rays. This effect is probably related to competing effects between prompt recombination and trapping (Cecilia *et al.*, 2009).

3.2. Spectral emission

The emission spectra were measured under X-ray irradiation (laboratory and synchrotron light sources) with a Hamamatsu R4632 photomultiplier tube coupled to an Oriel monochromator. The grating (77233 from Oriel) used has a 1200 lp/mm groove density and is blazed at 500 nm, which gives a primary wavelength range of 350 nm to 1200 nm. The system was controlled by a LabView program (NationalInstrument, last visit 2010). The scanning step size was 1 nm and the resolution of the system is 5 nm. The spectra were corrected for the grating wavelength response and the photomultiplier quantum efficiency.

3.2.1. Substrate During the project, two different substrate materials were developed at the CEA-Leti in Grenoble (France). In the following section we call them "Scin^{TAX} substrate 1" and "Scin^{TAX} substrate 2", respectively. Tests were carried out during the development of the substrates with a laboratory X-ray tube (Cu, W and Mo anode) at the ESRF. Further tests at the ANKA synchrotron light source were done under intense white beam radiation with energies in the range from 8 keV to 60 keV and flux densities of up to 10^{12} ph/s/mm^2.

From Figure 2, the substrate called "Scin^{TAX} substrate 2" was finally chosen for the epitaxy of LSO:Tb thin films, due to its total absence of luminescence (Fig. 2). Further details on this substrate are given in the corresponding patent application (Dupré *et al.*, submitted 2007, published 20th and 22th May 2009).

3.2.2. LSO-based thin film LSO:Tb SCF grown by LPE with Tb concentrations above 8% in the melt showed four strong emission lines under X-ray excitation (Fig. 3). These four lines correspond to the Tb^{3+} electronic transitions $^5D_4 \Rightarrow {}^7F_x$ (x = 6, 5, 4, 3). For Tb concentrations in the melt below 8%, additional lines (blue emission in the region 350 - 470 nm) appeared in the spectrum, corresponding to the electronic transitions $^5D_3 \Rightarrow {}^7F_x$, as shown in Fig. 4. These results are similar to those found by (Cooke, 2005) for bulk LSO:Tb crystals grown from the melt using the optical float-zone method, although Cooke's doping concentrations were much lower. Codoping of LSO:Tb layers with Ce^{3+} ions improves the scintillation efficiency: the Ce^{3+} ion adds a contribution peaked at 420 nm (Fig. 5) in the emission spectrum without quenching the emission due to Tb. This corresponds to the well-known transition from the 5d excited state to ^{2}F ground state of the Ce^{3+} ion. As outlined in section 3.1, the conversion yield is increased (compared to LSO:Tb).

The transmission of the substrate in the range [300 nm; 800 nm], to be shown later

within this article in detail, is close to 90% (cf. Fig. 4 and Fig. 5). We point out that there is no overlap between the LSO:Tb emission and the substrate absorption.

Emission spectra of LSO:Eu,Gd thin films show the transitions $^5D_0 \Rightarrow {}^7F_J$ (J=1, 2, 3, 4) from the Eu^{3+} ions (Cooke, 2005), as well as an emission peak at 320 nm due to the Gd^{3+} ions (Fig. 6). As discussed in section 3.1, the emission of LSO:Eu,Gd is poor compared to that of LSO:Tb(,Ce).

3.3. UV/visible light absorption

The setup applied for the investigations of visible light absorption used a Xenon lamp (emission range from 200 nm to 2400 nm) placed in an APEX illuminator (Newport). The lamp was coupled to a Cornerstone C260 monochromator with a 1200 l/mm grating blazed at 350 nm. After the monochromator output, the beam was split into two beams: the reflected beam was focused with a set of lenses onto a 918D-UV detector (Newport) as reference beam. The transmitted beam was focused on the sample under investigation via a set of lenses and its intensity measured with a 918D-UV detector (Newport). The system was controlled by a LabView program.

The linear attenuation coefficient (cm^{-1}) is calculated as follows:

$$\mu = \frac{1}{x} \times \log(\frac{I_0}{I}) \quad , \tag{3}$$

where x is the thickness of the crystal, I_0 is the intensity of the incident beam and I is the intensity of the transmitted beam through the sample. Substrates prepared from different crystal ingots were tested concerning UV/visible light absorption. They all showed absorption below 2 cm^{-1} in the visible range 300 nm to 700 nm, were LSO:Tb has its wavelengths of maximum emission. The substrate absorption coefficient spectrum presents an absorption band peaked at 255 nm which spreads between 200 nm and 280 nm. Hence, there is no re-absorption in the substrate of light emitted by the LSO:Tb layer (cf. Fig. 7).

Compared to the substrate alone, the absorption spectra of thick layers (overall absorption of the substrate plus the two layers at each side of the substrate) show a broadening of the absorption band. Furthermore, a shift of the peak to 261 nm, and the creation of a shoulder between 280 - 290 nm can be observed. This shoulder could be due to a Pb^{2+} incorporation into the layer, with the lead coming from the solvent used for the LPE growth (Martin *et al.*, 2009). For thin layers ($< 20\,\mu$m), the shoulder is not visible and the spectrum is similar to that of the substrate alone.

3.4. Afterglow

Afterglow is delayed luminescence from the scintillator occurring after the irradiation has stopped. This phenomenon is especially detrimental for fast X-ray imaging applications. The afterglow depends strongly on the exposure time and to a lesser extent on the X-ray photon flux density.

We measured the afterglow in the lab following a 10 s exposure to X-rays (Copper anode, 35 kV, 10 mA, X-ray flux density $\sim 10^6\ ph/mm^2/\mathrm{s}$). Measurements were performed with a Philips XP2020Q photomultiplier (PMT), a SR445 preamplifier and a SR400 gated photon counter (8 ms gating) both from Stanford Instruments. The thin crystal films were coupled to the PMT using an optical grease.

Following this exposure to X-rays, LSO:Tb thin films which were not thermally annealed were found to be compatible with operation over a 15bits dynamic range in 100 ms (Fig. 8). The thermal annealing of the LSO:Tb samples improves their conversion efficiency by as much as 30% but it also introduces more afterglow. Due to this effect, one can only exploit 11bits in 100 ms and 13bits in 1000 ms by using the annealed scintillator. The afterglow is also increased by Ge codoping (12% in the melt). LSO:Tb,Ge can only resolve 10bits in 100 ms and 12bits in 1000 ms. Codoping with Gd, with Ce or Pr did not introduce additional afterglow. LSO:Eu SCFs show

both a higher afterglow and a slow component (similar to the afterglow characteristics observed for LAG:Eu) compatible with only 9bits in 100 ms and 10bits in 1000 ms. Other parameters than thermal annealing and dopants (growth speed, growth temperature) do not play an important role concerning the afterglow of the LSO thin films in our investigations. Table 3 shows the dynamic range that can be exploited typically by common SCFs at the ESRF.

In synchrotron full-field X-ray micro-imaging, exposure times rarely exceed 10 s. However, the X-ray photon flux densities at synchrotron beamlines are several order of magnitudes higher than those used with lab X-ray-tubes.

3.5. Temperature effects

The temperature of the thin film scintillators can rise under the intense white radiation provided by synchrotron light sources (heat loads of up to 10 W/mm^2). The conversion efficiency of the SCF may change with temperature in a non-linear manner and also with dependency on the total irradiation time. High-speed tomography under white-beam synchrotron radiation requires that the conversion efficiency remains stable under high dose and high heat load.

In order to study the influence of temperature on the conversion efficiency, a Linkam system was applied (Linkam, last visit 2010). This consists of a temperature controlled HFS91 sample stage, a TMS94 PID controller which regulates the power supplied to a heating resistor, a LNP controller for the circulation of liquid nitrogen and a dewar. A thermocouple was placed in contact with the sample in order to register its temperature. The stage is designed for temperatures in the range -180^{o}C to 200^{o}C.

The light output from the crystal was recorded in transmission geometry with a photomultiplier (PMT). A thermocouple measured the temperature of the photomultiplier entrance window and was used to ensure that the photomultiplier was kept at room

temperature (RT). This was to avoid drifts of its response with respect to temperature. The X-rays were collimated by a set of slits (opening 1 mm × 1 mm) on the center of the 1" crystal. The light emitted by the scintillator was then focused onto the PMT cathode using two lenses each of focal length 75 mm. The current from the photomultiplier was measured by an electrometer and the analog voltage output of this fed into an analog input of the NI-DAQ 6052E acquisition card (NationalInstrument, last visit 2010). The current was recorded once the crystal temperature is stable, and results presented here were normalised with respect to the conversion efficiency at RT. The uncertainty on the conversion efficiency is ±3% in the worst case (this was evaluated experimentally by measuring the temperature response of a reference crystal every day over several weeks). For the measurements, we used an X-ray generator equipped with a copper anode operated at 20 kV and 45 mA, no absorption filter.

Results show that the conversion efficiency from LSO:Tb decreases by nearly 20% from RT to 180^{o}C (Fig. 9). Its conversion efficiency is nearly constant from RT to 50^{o}C, in contrast to LAG:Sc,Eu which shows a 10% decrease over the same temperature interval.

The dependence of the conversion efficiency on the temperature did not change by varying the growth parameters or thickness of the films. The only exception was the codoping with cerium, which changed slightly the shape of the temperature response (Fig. 10).

The decrease in the conversion of LSO:Tb with temperature was also investigated via its emission spectrum (Fig. 11) by placing a monochromator between the optics and the photomultiplier. By integrating the area under the emission spectrum over the wavelength range (Light Yield), we found a 18.5% decrease of the conversion efficiency between RT and 180^{o}C, which is in agreement with our previous estimation of a 20% decrease (Fig. 10).

The conversion efficiency of LSO:Tb thin films was found to increase with temperatures below 0^{o}C. At -100^{o}C, the conversion efficiency was 50% higher than at RT (Fig. 12).

4. Performance

An indirect X-ray imaging system comprises several components. Our system includes a thin film scintillator, visible light optics (microscope objective, mirror and eyepiece) and a CCD detector. The components must be adapted with respect to each other in order to maximise the overall performance of the detection system.

4.1. Spectral Matching Factor

A crucial parameter of an indirect X-ray imaging system based on a scintillating screen is the optical match between the scintillation spectrum and the CCD quantum efficiency. This parameter can be quantified through the spectral matching factor (SMF), which is defined by the ratio:

$$\mathrm{SMF} = \frac{\int \mathrm{QE}(\lambda) \cdot S_{scint}(\lambda)\ \mathrm{d}\lambda}{\int S_{scint}(\lambda)\ \mathrm{d}\lambda} \quad . \tag{4}$$

$QE(\lambda)$ is the quantum efficiency of the CCD camera at the wavelength λ and $S_{scint}(\lambda)$ is the relative efficiency of the scintillator at the wavelength λ normalised with respect to the maximum intensity of the spectrum. Based on this definition, the SMF is a figure of merit which quantifies the compatibility of the scintillator with a given CCD camera.

Table 4 shows the SMF obtained for different combinations of scintillators with CCD cameras. The emission spectra of the scintillators were obtained under exposition to X-rays from a tungsten anode. The quantum efficiencies of the two CCD cameras under study are plotted in Fig. 13, as well as the emission spectra of LSO:Tb and GGG:Eu

thin films. The measured spectra are convoluted with the quantum efficiency of the different CCD cameras.

We found that the GGG:Eu emission spectrum is the best adapted for use with a FReLoN 2k14bit camera (equipped with a front-illuminated TH7899M e2v chip – former Atmel). On the contrary, LSO:Tb is the best choice with a PCO SensicamQE camera (equipped with a ICX285AL Sony interline transfer sensor). In a more general way, we can say that the LSO:Tb can be optimally coupled to interline or back-illuminated CCD cameras, for which the quantum efficiency peak is in the blue region of the visible spectrum (400 nm - 550 nm). Back-illuminated CCDs show almost ideal spectral response (a higher overall QE which expands to the near UV region), this is because the visible photons impinge directly on the sensitive Si layer of the chip. Interline CCD chip technology typically shows a peak in the spectral response between 400 nm and 500 nm and low quantum efficiency beyond 600 nm. On the other hand, GGG:Eu is compatible with front-illuminated CCD cameras, for which the quantum efficiency peaks in the red region (600 nm - 800 nm) of the visible spectrum. In a front-illuminated CCD, photons enter the Si substrate of the chip through poly-Si electrodes, which absorb or reflect a significant fraction of the incident short wavelength photons. As a result, the quantum efficiency of front-illuminated CCD chips is low below 400 nm and generally peaks between 600 nm and 800 nm.

4.2. Light Collection Efficiency

In a high resolution X-ray imaging system, the optics frequently consist of a microscope objective and possibly an additional eyepiece plus mirror to realize a folded optical beam path. This optical system is placed between the SCF and the CCD camera (see Fig. 1).

The collection efficiency η_{coll} of the optics depends upon the Numerical Aperture

NA of the microscope objective and the refractive index $n(\lambda_{em})$ of the SCF at the emission wavelength λ_{em}:

$$\eta_{coll} = \frac{1}{4}\left(\frac{\mathrm{NA}}{n(\lambda_{em})}\right)^2 \quad . \tag{5}$$

Therefore, to optimise the light collection efficiency, the NA should be high and the SCF's refractive index should be as low as possible.

The refractive index of the LSO:Tb SCF was measured by the prism coupling method (m-lines) (Onodera *et al.*, 1983) at the Claude Bernard University in Lyon. The results are shown in table 5 together with the refractive index of representative SCFs at their wavelengths of maximum emission. A point to be stressed is that the values of the refractive index of the SCIN^{TAX} substrate (1.83) and the LSO:Tb layers (1.82) were found to be very close, indicating that the light transmission at the layer/substrate interface is maximised. In addition the refractive index of the SCIN^{TAX} substrate is significantly smaller than the GGG substrate resulting in a better collection efficiency of the optics (14% gain).

4.3. Detector Efficiency

The LSO:Tb X-ray efficiency dependence on the photon energy was measured between 8 keV and 60 keV at the beamline BM05 of the ESRF (Ziegler *et al.*, 2004), for two different X-ray imaging systems. One system is based on the SensicamQE (ICX285AL Sony) interline transfer CCD camera and the other is based on the FReLoN 2k (TH7899 e2v sensor) front-illuminated CCD. Both systems were coupled to an optics consisting of a 4x objective (NA=0.16) from Olympus. In Fig. 14 the LSO:Tb efficiency values are reported normalised to those of the GGG:Eu performance. The latter is currently the state-of-the-art thin film scintillator for high resolution hard X-ray imaging with indirect detection schemes used at the ESRF. Both, the GGG:Eu and LSO:Tb SCFs used for the measurements had the same thick-

ness of 5 μm. Results show that the LSO:Tb combined with the PCO SensicamQE has the best performance up to 55 keV. However, when using a FReLoN 2k, the performance is better than GGG:Eu up to only 20 keV. This is in contradiction to the theoretical stopping power of the LSO material and could be related to light yield non-proportionality which is already known for LSO:Ce scintillators (Dorenbos, 2002).

4.4. Line Spread Function

The achievable spatial resolution of different detector-scintillator combinations was evaluated at an X-ray energy of 24 keV at the Topo-Tomo beamline of the ANKA synchrotron in Karlsruhe. A 10x Olympus objective with NA=0.4 was used. A 2.5x eyepiece was added to project the visible light image onto a PCO4000 CCD camera. The pixel size of the camera is $9\,\mu$m **giving a nominal input pixel size of** $0.36\,\mu$m**. The spatial resolution limit given by the optics is in this case** $0.83\,\mu$m**. The Line Spread Function (LSF) was measured with a cleaved GaAs edge. The edge was imaged with a slight angle with respect to the vertical axis and the slanted edge plugin from ImageJ was used to perform the LSF calculation from the image. Fig. 16 gives a comparison of the LSFs from a LSO:Tb SCF on its substrate and a LAG:Eu SCF on its YAG substrate. The YAG substrate is known to emit intrinsic scintillation light. We used a FGL495 filter (Thorlabs) to cut this parasitic emission below 500 nm. However, the remaining scintillation from the substrate induces a tail on the LSF. This effect becomes worse as the X-ray energy is increased. The FWHM of the LSF for the LSO:Tb SCF is 3 pixels (corresponding to** $1.1\,\mu$m**) and the full width (intensity divided by 10) is 10 pixels (corresponding to** $3.6\,\mu$m**). The benefit of the substrate developed during the Scin$^{\mathrm{TAX}}$ project is demonstrated here by the decreas-**

ing of the tail in the LSF. The spatial resolution can be further enhanced by using a thinner crystal (FWHM=0.94 μm with a 5 μm thick crystal) in order to fit with the depth of focus of the objective (here 3 μm), but at the expense of efficiency.

5. Application

As an example of an application we have chosen a biological specimen. Biological samples are frequently characterised by weak X-ray absorption and consequently a high image contrast is required in order to identify their smallest features. Furthermore for the specimen chosen, a detector with high efficiency in combination with spatial micro-resolution was required in order to reduce the dose which would otherwise damage the organic sample.

The scientific interest is the study of evolutions in animal anatomy which are often focused on the morphology of body appendages. The leg of the honey bee (*apis mellifera*) is such an appendage of arthropods, a phylum with over two million species, whose diversity is characterized by the number, morphology and function of these jointed attachments called appendages (Shubin *et al.*, 1997). In the class of insects there exists a great variation of legs. All insects like honey bees have three pairs of legs. These legs can be variously modified depending on their function like walking, running, jumping, digging, grabbing, swimming, transporting or producing and sensing vibrations (Kilpinen & Storm, 1997), (Sandeman *et al.*, 1996). Basically each leg has 6 segments (Cook, 1888). The *coxa* connects the leg to the *thorax*. Distal to the *coxa* are the segments: *trochanter*, *femur*, *tibia*, and *tarsus*. Furthermore such segments in the hind legs perform specific functions like the pollen brush on the inner surface of the first tarsal segment, the pollen packer in the joint between the tibia and the first tarsal segment and the pollen basket (*corbicula*) on the outer surface of the tibia.

With notches in the first tarsal segments of the prothoracic legs the honey bee can clean its *antennae* (Winston, 1991).

5.1. X-ray imaging system

Experiments were carried out at the beamline ID22 of the European Synchrotron Radiation Facility ESRF. The high-resolution X-ray imaging system used comprises a 10 μm thick LSO:Tb single crystal film grown on a SCIN^{TAX} substrate (8 mm x 8 mm, 160 μm thick), a FReLoN CCD camera (e2v chip TH7899M) and a diffraction limited visible light microscope manufactured by the French company OptiquePeter. The latter was equipped with a 10x Olympus objective (NA=0.4), and a 2x magnification eyepiece. The pixel size of the FReLoN's CCD chip is 14 μm. The effective pixel size of the detector was therefore $\sim$0.7 μm, giving a spatial resolution limit of R $>$ 1.4 μm, according to Shannon's theorem. **The spatial resolution at the given energy was verified with a test pattern (Xradia Inc., model X500-200-30): see inset of Figure 15 (the resolution limit of the optics was 0.9 μm). For further details about the micro-imaging station of the ID22 beamline the reader is referred to the literature (Weitkamp *et al.*, 1999).**

5.2. Microtomography

For the high resolution tomography scan an X-ray energy of 8 keV was selected with a double-crystal monochromator and a mirror. No additional X-ray filters were used. The sample-to-detector distance was 11 mm. 1500 projection images were acquired by rotating the sample stepwise over 180°. In addition, 21 dark- and 42 flat-field images were acquired for intensity normalisation purposes. With an exposure time of 0.3 s the total acquisition lasted 8 min. The three dimensional image of the honey bee leg was reconstructed by using the filtered back-projection algorithm via the ESRF software

package PyHST (Mirone *et al.*, 2010).

Considering the light output of the $10\,\mu$m **scintillator (40 ph/keV) and its absorption at 8 keV (59%), the number of visible light photons created at 8 keV per incident X-ray photon approaches 190. Those 190 photons per X-ray photon are then emitted through the optics towards the detector. The collection efficiency of the optics in our case is 0.96% (cf. section 4.2. for the calculation), which means that only 1.8 visible light photons per X-ray will reach the CCD chip. Taking into account the 23.4% spectral matching factor of the CCD camera and if we consider that the transmission through the optics is 100% (approximation), we calculate that 0.43 electron-hole pairs per 8 keV X-ray photon will be created in the CCD. It means 1.2** $\times$ $\mathbf{10^6}$ **ph/s are registered in one pixel, assuming a photon flux density of** $\sim\mathbf{10^{11}}$ ph/mm^2**/s and a pixel surface of** $0.313\,\mu\mathrm{m}^2$**. As the pixel well depth is 300 000 electrons, the acquisition time to saturate the CCD camera is 0.25 s, which is close to the experimental exposure time mentioned above.**.

Figure 15 shows the rendering of a part of the foot (*tarsus*) with claws located at its end. Between the claws a flexible pad, the *arolium*, is situated, which enables the bee to adhere to smooth surfaces (Federle *et al.*, 2001), (Gorb, 2008). These structural and biophysical insights of insect legs facilitate bionic applications (Delcomyn *et al.*, 1996), (Vella, 2008). The tomographic approach opens new possibilities of morphometric characterization (Nickel *et al.*, 2008). Further possibilities of synchrotron radiation based microtomography for life sciences applications are discussed in the literature (Betz *et al.*, 2007).

6. Conclusion

LSO epitaxial layers were successfully grown for the first time on suitably adapted substrates by Liquid Phase Epitaxy. The innovative substrates developed within the Scin^{TAX} project are, unlike common substrates such as YAG or GGG, free from intrinsic luminescence. This improves the resolution of the thin films, especially for film thicknesses below 20 μm and at high energies above 20 keV for which only a small fraction of the X-rays are absorbed in the thin films.

Only Eu^{3+}, Tm^{3+} and Tb^{3+} could be tested as single dopants in the LSO lattice. For other dopants (e. g., Ce^{3+}, Pr^{3+}) the lattice mismatch between the substrate used and the epitaxial film was too high or the segregation coefficient was too low, resulting in the growth of layers with poor optical quality. Tb^{3+} is the most efficient dopant in the LSO lattice for thin films and its emission at 550 nm is well matched to most CCD cameras. With front-illuminated cameras such as the FReLoN 2k (e2v chip TH7899M), the GGG:Eu SCF which has its emission spectrum in the red region is still the best compromise for X-ray energies below 63 keV. The LSO:Tb single crystal films present higher conversion efficiency and better X-ray absorption efficiency than the YAG:Ce, LAG:Eu, LAG:Tb or GGG:Eu thin films that were developed in the past. If LSO:Tb, which has its emission spectrum in the green region, is used in combination with interline transfer or front-illuminated CCDs (like the PCO Sensicam studied in this paper), it will further improve the overall efficiency of current X-ray micro-imaging systems. Ce^{3+} can be used as a codopant to further improve the conversion efficiency without increasing the afterglow. Moreover, the LSO:Tb thin film will suit perfectly the new generations of CCD cameras developed at the ESRF which are based on back-illuminated sensors.

Acknowledgements The Scin^{TAX} project is funded by the European community

(STRP 033 427) as part of the Sixth Framework Programme (FP6). We thank Eric Ziegler, scientist in charge of the ESRF beamline BM05, for giving us the opportunity to test scintillators on high resolution detectors. We thank Jeremy Merlin (CEA-Leti, Grenoble) for the high precision polishing work on crystals and Anne Pillonnet (CNRS, Lyon) for the refractive index measurements. We thank the members of the detector group at the ESRF, especially Francis Lesimple and Christophe Jarnias, who contributed to the measurements presented in this paper. A particular 'thank you' goes to John Morse from the detector group of the ESRF, who kindly gave extensive advices for the finalisation of this article.

References

Banhart, J. (ed.) (2008). *Advanced Tomographic Methods in Materials Research and Engineering*. Oxford University Press.

Baruchel, J., Buffiere, J.-Y., Cloetens, P., Di Michiel, M., Ferrie, E., Ludwig, W., Maire, E. & Salvo, L. (2006). *Scripta Mater.* **55**, 41–46.

Baruchel, J., Cloetens, P., Härtwig, J. & Schlenker, M. (2002). In *Third-Generation Hard X-Ray Synchrotron Radiation Sources*, edited by D. M. Mills, chap. Imaging with Third-Generation Synchrotron X-Rays, pp. 181–202. John Wiley & Sons, Inc., New York.

Beckmann, F., Lippmann, T., Metge, J., Dose, T., Donath, T., Tischer, M., Liss, K. D. & Schreyer, A. (2004). In *AIP Conference Proceedings (SRI2003)*, vol. 708, pp. 392–395.

Betz, O., Wegst, U., Weide, D., Heethoff, M., Helfen, L., Lee, W. & Cloetens, P. (2007). *J. Microsc.* **227**, 51.

Bleuet, P., Cloetens, P., Gergaud, P., Mariolle, D., Chevalier, N., Tucoulou, R., Susini, J. & Chabli, A. (2009). *Rev. Sci. Instrum.* **80**(5), 056101.

Bonse, U. & Busch, F. (1996). *Prog. Biophys. Molec. Biol.* **65**, 133–169.

Bonse, U., Nusshardt, R., Busch, F., Pahl, R., Johnson, Q. C., Kinney, J. H., Saroyan, R. A. & Nichols, M. C. (1989). *Rev. Sci. Instrum.* **60**(7), 2478–2481.

Born, M. & Wolf, E. (1999). *Principles of Optics*. Cambridge University Press, 7th ed.

Cecilia, A., Rack, A., Douissard, P.-A., Martin, T., dos Santos Rolo, T., Vagovič, P., Pelliccia, D., Baumbach, T., Couchaud, M. & Dupré, K. (2010). *Nucl. Instr. & Meth. in Phys. Res. B*, **inprint**, DOI 10.1016/j.nima.2010.06.192.

Cecilia, A., Rack, A., Pelliccia, D., Douissard, P.-A., Martin, T., Couchaud, M., Dupré, K. & Baumbach, T. (2009). *Rad. Eff. Def. Solids*, **164**(9), 517–522.

Chapman, D., Thomlinson, W., Johnston, R. E., Washburn, D., Pisano, E., Gmür, N., Zhong, Z., Menk, R., Arfelli, F. & Sayers, D. (1997). *Phys. Med. Biol.* **42**(11), 2015.

Cloetens, P., Barrett, R., Baruchel, J., Guigay, J.-P. & Schlenker, M. (1996). *J. phys. D, Appl. phys.* **29**(1), 133–146.

Cloetens, P., Ludwig, W., Baruchel, J., Dyck, D. V., Landuyt, J., Guigay, J. P. & Schlenker, M. (1999). *Appl. Phys. Lett.* **75**, 2912–2914.

Cook, A. (1888). *American Naturalist*, pp. 193–201.

Cooke, D. W. (2005). *Opt. Mater.* **27**, 1781–1786.

Delcomyn, F., Nelson, M. & Cocatre-Zilgien, J. (1996). *Inter. J. Robotics Res.* **15**, 113.

Derenzo, S. E., Weber, M. J., Bourret-Courchesne, E. & Klintenberg, M. K. (2003). *Nucl. Instr. & Meth. in Phys. Res. A*, **505**, 111–117.

Di Michiel, M., Merino, J. M., Fernandez-Carreiras, D., Buslaps, T., Honkimäki, V., Falus, P., Martins, T. & Svensson, O. (2005). *Rev. Sci. Instrum.* **76**, 043702–1–043702–7.

Dorenbos, P. (2002). *Nucl. Instr. & Meth. in Phys. Res. A*, **486**(1–2), 208–213.

Dupré, K., Couchaud, M., Martin, T. & Rack, A. (submitted 2007, published 20th and 22th May 2009). *German Patent Application submitted: ref. no. DE 10 2007 054 700.7, published: DE102007054700 (A1) and WO2009062831 (A1).*

Federle, W., Brainerd, E., McMahon, T. & Hölldobler, B. (2001). *Proc. Nat. Acad. Sci.* **98**, 6215.

Ferrand, B., Chambaz, B. & Couchaud, M. (1999). *Opt. Mater.* **11**, 101–114.

Feser, M., Gelb, J., Chang, H., Cui, H., Duewer, F., Lau, S. H., Tkachuk, A. & Yun, W. (2008). *Meas. Sci. & Tech.* **19**(9), 094001.

Flannery, B. P., Deckmann, H. W., Roberge, W. G. & D'Amico, K. L. (1987). *Science*, **237**(4821), 1439–1444.

García-Moreno, F., Rack, A., Helfen, L., Baumbach, T., Zabler, S., Babcsán, N., Banhart, J., Martin, T., Ponchut, C. & Di Michiel, M. (2008). *Appl. Phys. Lett.* **92**, 134104–1–134104–3.

Gorb, S. (2008). *Insect Mech. & Control*, **34**, 81–116.

Graafsma, H. & Martin, T. (2008). In *Advanced Tomographic Methods in Materials Research and Engineering*, edited by J. Banhart. Oxford University Press.

Graeff, W. & Engelke, K. (1991). In *Handbook on Synchrotron Radiation*, edited by S. Ebashi, M. Koch & E. Rubenstein, vol. 4, chap. Microradiography and Microtomography, pp. 361–406. North-Holland; Amsterdam, Oxford, New York, Tokyo.

Hartmann, W., Markewitz, G., Rettenmaier, U. & Queisser, H. J. (1975). *Appl. Phys. Lett.* **27**, 308–309.

Khartsev, S. & Grishin, A. (2005). *Appl. Phys. Lett.* **86**.

Kilpinen, O. & Storm, J. (1997). *Journal of Comparative Physiology A: Neuroethology, Sensory, Neural, and Behavioral Physiology*, **181**, 309–318.

Kinney, J. H., Johnson, Q. C., Nichols, M. C., Bonse, U., Saroyan, R. A., Nusshardt, R. & Pahl, R. (1989). *Rev. Sci. Instrum.* **60**(7), 2471–2474.

Koch, A. (1994). *Nucl. Instr. & Meth. in Phys. Res. A*, **348**, 654–658.

Koch, A., Cloetens, P., Ludwig, W., Labiche, J. C. & Ferrand, B. (1999*a*). Proceeding of the Fifth International Conference on Inorganic Scintillators and their Applications – SCINT99.

Koch, A., Peyrin, F., Heurtier, P., Ferrand, B., Chambaz, B., Ludwig, W. & Couchaud, M. (1999*b*). In *Physics of Medical Imaging*, edited by J. M. Boone & J. T. Dobbins III, vol. 3659 of *Proc. of SPIE*, pp. 170–179.

Koch, A., Raven, C., Spanne, P. & Snigirev, A. (1998). *J. Opt. Soc. Am.* **15**, 1940–1951.

Labiche, J.-C., Mathon, O., Pascarelli, S., Newton, M. A., Ferre, G. G., Curfs, C., Vaughan, G., Homs, A. & Carreiras, D. F. (2007). *Rev. Sci. Instrum.* **78**, 0901301.

Lee, H.-R., Lai, B., Yun, W., Mancini, D. C. & Cai, Z. (1997). In *Developments in X-ray Tomography*, edited by U. Bonse, vol. 3149 of *Proc. of SPIE*, pp. 257–264.

Linkam, (last visit 2010). *Linkam Web Site*. `http://linkam.co.uk`.

Lübbert, D., Baumbach, T., Härtwig, J., Boller, E. & Pernot, E. (2000). *Nucl. Instr. Meth. B*, **160**(4), 521–527.

Ludwig, W., Cloetens, P., Härtwig, J., Baruchel, J., Hamelin, B. & Bastie, P. (2001). *J. Appl. Cryst.* **34**(5), 602–607.

Martin, T., Couchaud, M., Ferrand, B., Caillet, A., Pelenc, D., Chambaz, B. & Passero, A. (2005). Proceeding of the Eighth International Conference on Inorganic Scintillators and their Applications – SCINT2005.

Martin, T., Douissard, P.-A., Couchaud, M., Cecilia, A., Baumbach, T., Dupré, K. & Rack, A. (2009). *IEEE Trans. Nucl. Sci.* **56**(3), 1412–1416.

Martin, T. & Koch, A. (2006). *J. Synchrotron Rad.* **13**, 180–194.

Mirone, A., Wilcke, R., Hammersley, A. & Ferrero, C., (2010). *PyHST – High Speed Tomographic Reconstruction.* `http://www.esrf.eu/UsersAndScience/Experiments/TBS/SciSoft/`.

Modregger, P., Lübbert, D., Schäfer, P. & Köhler, R. (2007). *Appl. Phys Lett.* **90**, 193501.

NationalInstrument, (last visit 2010). *National Instrument Web Site*. `http://ni.com`.

Nickel, M., Hammel, J., Herzen, J., Bullinger, E. & Beckmann, F. (2008). In *Developments in X-ray Tomography VI*, edited by S. R. Stock, vol. 7078 of *Proc. of SPIE*, pp. 70781W–70781W.

Nugent, K. A., Gureyev, T. E., Cookson, D. F., Paganin, D. & Barnea, Z. (1996). *Phys. Rev. Lett.* **77**, 2961–2964.

Onodera, H., Awai, I. & Ikenoue, J.-I. (1983). *Appl. Opt.* **22**(8), 1194–1197.

Ortega, R., Cloetens, P., Devès, G., Carmona, A. & Bohic, S. (2007). *PLoS ONE*, **2**(9), e925.

Rack, A., García-Moreno, F., Baumbach, T. & Banhart, J. (2009*a*). *J. Synchrotron Radiat.* **16**(3), 432–434.

Rack, A., Weitkamp, T., Bauer Trabelsi, S., Modregger, P., Cecilia, A., dos Santos Rolo, T., Rack, T., Haas, D., Simon, R., Heldele, R., Schulz, M., Mayzel, B., Danilewsky, A. N., Waterstradt, T., Diete, W., Riesemeier, H., Müller, B. R. & Baumbach, T. (2009*b*). *Nucl. Instr. & Meth. in Phys. Res. B*, **267**(11), 1978–1988.

Rack, A., Zabler, S., Müller, B., Riesemeier, H., Weidemann, G., Lange, A., Goebbels, J., Hentschel, M. & Görner, W. (2008). *Nucl. Instr. & Meth. in Phys. Res. A*, **586**(2), 327–344.

Reznikova, E., Weitkamp, T., Nazmov, V., Last, A., Simon, M. & Saile, V. (2007). *Physica stat. sol. A*, **204**, 2811–2816.

Sandeman, D., Tautz, J. & Lindauer, M. (1996). *J. Exp. Biol.* **199**, 2585–2594.

Schroer, C. G., Meyer, J., Kuhlmann, M., Benner, B., Günzler, T. F., Lengeler, B., Rau, C., Weitkamp, T., Snigirev, A. & Snigireva, I. (2002). *Appl. Phys. Lett.* **81**(8), 1527–1529.

Shannon, C. E. & Weaver, W. (1963). *Mathematical Theory of Communication*. University of Illinois Press.

Shubin, N., Tabin, C. & Carroll, S. (1997). *Nature*, **388**, 639–648.

Snigirev, A., Snigireva, I., Kohn, V. & Kuznetsov, S. (1995). *Rev. Sci. Instrum.* **66**(12), 5486–5492.

Spanne, P. & Rivers, M. L. (1987). *Nucl. Instr. & Meth. Phys. Res. B*, **24-25**, 1063–1067.

Spiller, E. (1980). *Nucl. Instr. & Meth.* **177**(1), 187–192.

Stampanoni, M., Borchert, G. & Abela, R. (2005). *Nucl. Instr. & Meth. in Phys. Res. A*, **551**(1), 119–124.

Stampanoni, M., Borchert, G., Wyssc, P., Abela, R., Patterson, B., Hunt, S., Vermeulen, D. & Rüegsegger, P. (2002). *Nucl. Instr. & Meth. in Phys. Res. A*, **491**, 291–301.

Stampanoni, M., Groso, A., Isenegger, A., Mikuljan, G., Chen, Q., Meister, D., Lange, M., Betemps, R., Henein, S. & Abela, R. (2007). In *AIP Conference Proceedings (SRI2006)*, edited by J.-Y. Choi & S. Rah, vol. 879, pp. 848–851.

Stock, S. (1999). *Internat. Mater. Rev.* **44**(4), 141–164.

Stock, S. (2008). *Internat. Mater. Rev.* **53**(3), 129–181.

Uesugi, K., Suzuki, Y., Takano, H., Tamura, S., Kamijo, N. & Yagi, N. (2004). In *AIP Conference Proceedings (SRI2003)*, vol. 708, pp. 1316–1319.

Vella, D. (2008). *Langmuir*, **24**, 8701–8706.

Wang, Y., De Carlo, F., Mancini, D. C., McNulty, I., Tieman, B., Bresnahan, J., Foster, I., Insley, J., Lange, P., Laszewski, G., Kesselmann, C., Su, M.-H. & Thibaux, M. (2001). *Rev. Sci. Instrum.* **72**(4), 2062–2068.

Wang, Y., Liu, X., Im, K.-S., Lee, W.-K., Wang, J., Fezzaa, K., Hung, D. L. S. & Winkelman, J. R. (2008). *Nature Phys.* **4**, 305–309.

Weber, M. (2002). *J. Luminesc.* **100**, 35–45.

Weitkamp, T., Raven, C. & Snigirev, A. A. (1999). In *Developments in X-ray Tomography II*, edited by U. Bonse, vol. 3772 of *Proc. of SPIE*, pp. 311–317.

Winston, M. (1991). *The biology of the honey bee*. Harvard University Press.

www.crytur.cz, (last visit 2010). *Crytur Web Site*. `http://www.crytur.cz`.

www.scintax.eu, (last visit 2010). *ScinTax – Novel ceramic thin scintillator for high resolution X-ray imaging*. `http://www.scintax.eu`.

Ziegler, E., Hoszowska, J., Bigault, T., Peverini, L., Massonnat, J. Y. & Hustache, R. (2004). In *SYNCHROTRON RADIATION INSTRUMENTATION: Eighth International Conference on Synchrotron Radiation Instrumentation (SRI03)*, edited by T. Warwick, J. Stohr, H. A. Padmore & J. Arthur, vol. 705 of *AIP Conf. Proc.*, pp. 436–439.

Table 1. *Properties of SCF materials frequently used at the ESRF.*

	YAG:Ce	LAG:Eu	LAG:Tb	GGG:Eu
Conversion Efficiency [% of bulk YAG:Ce]	60%	30%	50%	90%
ρ [g/cm^3]	4.5	6.6	6.6	7.1
Z_{eff}	32	63	63	53
Max. Emission Wavelength [nm]	550	550, 750	350, 700	550, 750
Afterglow 20 ms after 0.1 s exposure	0.1%	1%	0.7%	0.1%
Afterglow 100 ms after 0.1 s exposure	0.06%	0.03%	0.1%	0.001%
Luminescence of substrate	Yes (YAG)	Yes (YAG)	Yes (YAG)	Slight (GGG)

Table 2. *Conversion efficiency of the thin screens developed within the Scin^{TAX} project. The efficiency is normalized with respect to the conversion efficiency of bulk YAG:Ce.*

Scintillator	Max. Conversion Efficiency (relative to YAG:Ce) η_{max}
Lu_2SiO_5:Eu,Gd,Ge,Y	30
Lu_2SiO_5:Tb	130
Lu_2SiO_5:Tb,Eu	70
Lu_2SiO_5:Tb,Eu,Tm	40
Lu_2SiO_5:Tb,Eu,Tm,Ce	40
Lu_2SiO_5:Tb,Ce	150
Lu_2SiO_5:Tb,Gd	140
Lu_2SiO_5:Tb,Ge	130
Lu_2SiO_5:Tb,Pr	22
Lu_2SiO_5:Tb,Sm	15
Lu_2SiO_5:Tb,Cr	130

Table 3. *Dynamic range exploitable by common thin film scintillators used in synchrotron radiation facilities, following 10 s exposure to X-rays (Cu anode, 35 kV, 10 mA). The afterglow is registered 100 ms and 1000 ms after the exposure to X-rays.*

SCF	Dynamic Range (100 ms)	Dynamic Range (1000 ms)
YAG:Ce	8 bit	9 bit
LAG:Eu (annealed)	9 bit	10 bit
GGG:Eu (annealed)	12 bit	14 bit

Table 4. *Spectral Matching Factor (SMF) for different combinations of CCD cameras and SCFs.*

SCF	FReLoN 2k (ESRF)	Sensicam SVGA (PCO)	SensicamQE (PCO)
YAG:Ce	0.269	0.262	0.450
GGG:Eu	0.332	0.192	0.317
LAG:Eu	0.327	0.192	0.332
LSO:Tb	0.234	0.295	0.496
LSO:Eu,Gd	0.300	0.229	0.407

Table 5. *Comparison of the maximum emission wavelength and refractive index of SCFs.*

SCF	Max. Emission Wavelength λ [nm]	Refractive Index $n(\lambda)$
$Y_3Al_5O_{12}$:Ce	550	1.83
$Gd_3Ga_5O_{12}$:Eu	710	1.96[a]
$Lu_3Al_5O_{12}$:Eu	710	1.85
Lu_2SiO_5:Tb Scin^{TAX}	550	1.82

[a] 1.96 is the refractive index of undoped GGG, found in literature (Khartsev & Grishin, 2005)

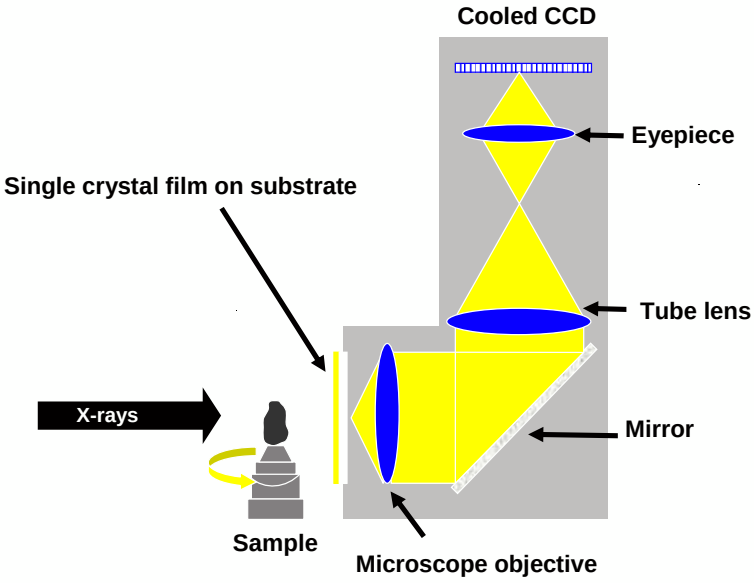

Fig. 1. Principle of a indirect high-resolution X-ray imaging system with folded optics, widely used in synchrotron-based hard X-ray imaging.

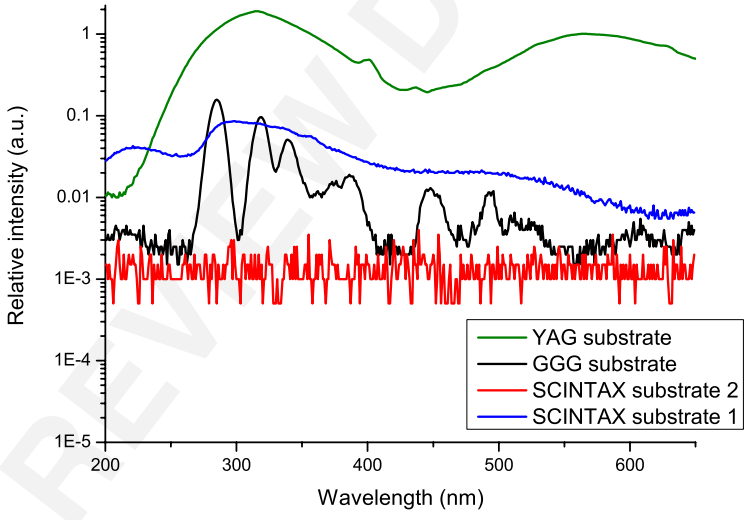

Fig. 2. Comparison of the luminescence of different substrates (YAG, GGG, Scin^{TAX}) under 40 kV, 40 mA X-ray irradiation using a Mo anode. Note: the vertical axis is plotted in logarithmic scale.

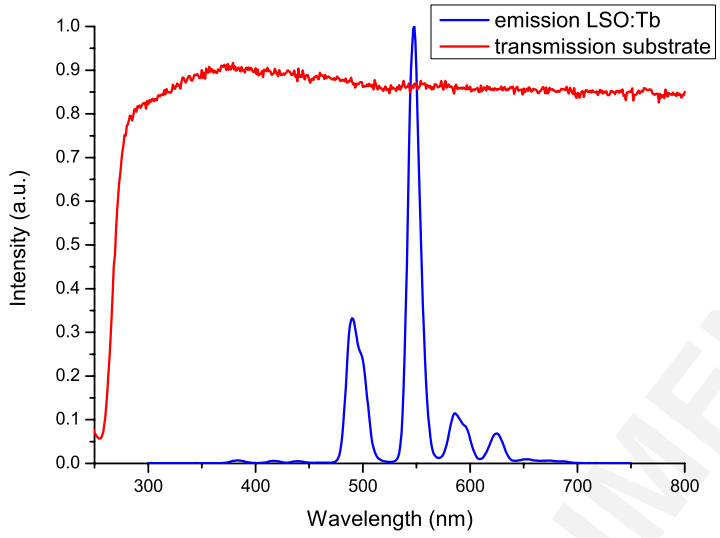

Fig. 3. Emission spectrum of LSO:Tb (15% Tb in the melt) with peak emission at 550 nm and the transmission of the substrate in the wavelength range from 250 nm to 800 nm.

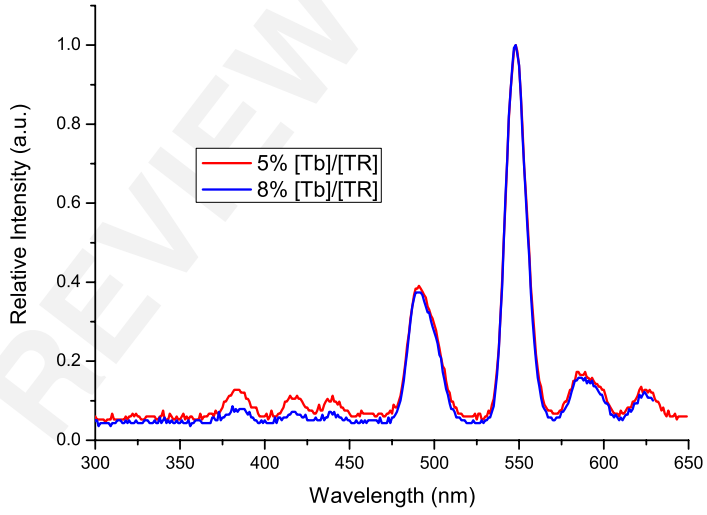

Fig. 4. Emission spectrum of LSO:Tb for 5% and 8% concentration of Tb in the melt, respectively.

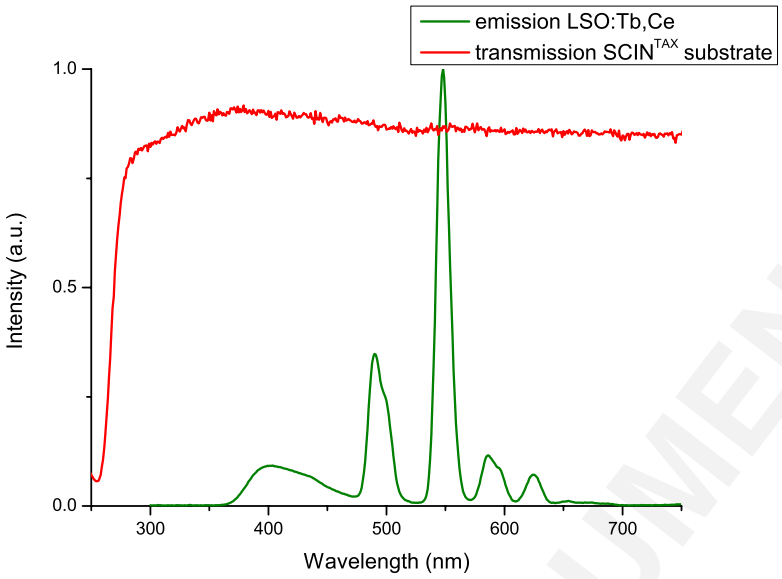

Fig. 5. Emission spectrum of LSO:Tb,Ce with peak emission at 550 nm and transmission curve of the substrate in the wavelength range from 250 nm to 800 nm. Note the additional luminescence band peaking at 420 nm, due to Ce^{3+} codoping.

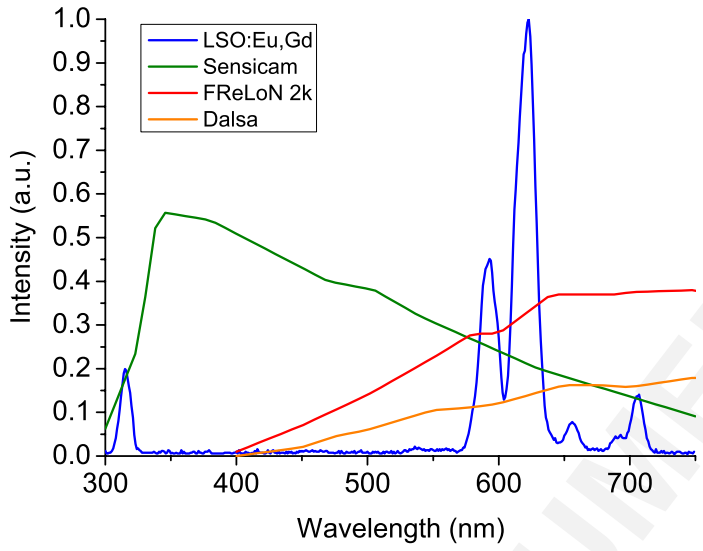

Fig. 6. Emission spectrum of LSO:Eu,Gd with peak emission at 610 nm. The quantum efficiency curves of three CCD cameras (PCO Sensicam SVGA, FReLoN 2k and Dalsa 1M60) are plotted in the same graph. LSO:Eu,Gd emission is best adapted for front-illuminated cameras such as the FReLoN 2k or Dalsa 1M60.

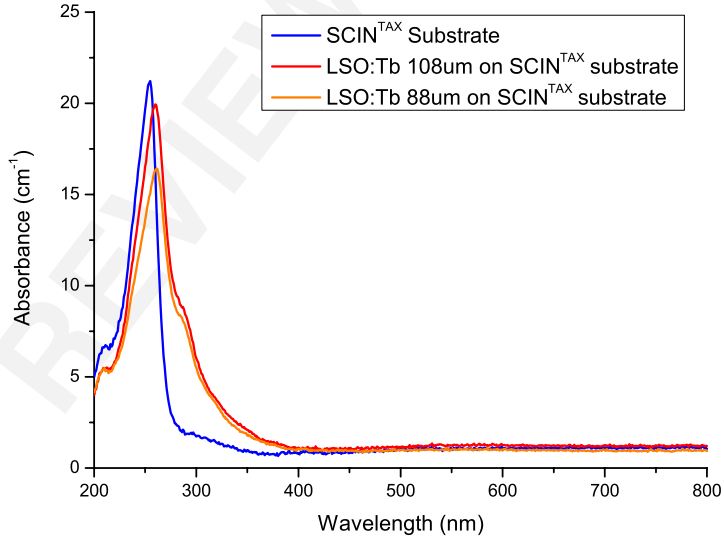

Fig. 7. Absorption spectra of the substrate alone (blue curve); 88 μm thick LSO:Tb layer on substrate (red); 108 μm thick LSO:Tb layer on substrate (orange).

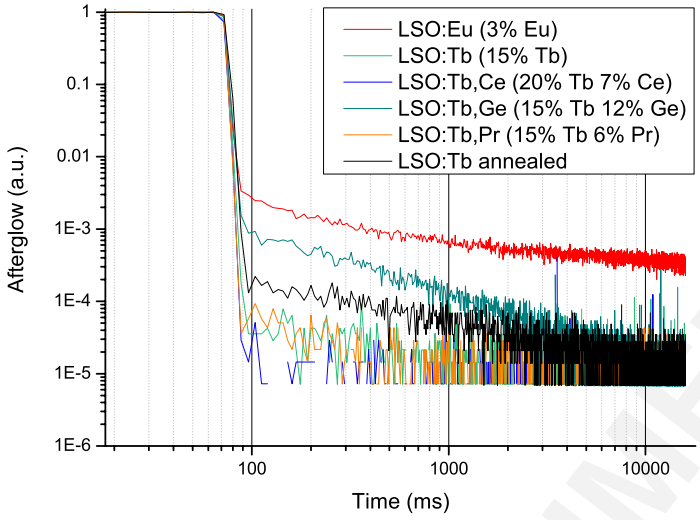

Fig. 8. Influence of the dopant combination on the afterglow of the LSO thin films. Note the increase of the afterglow for annealed LSO:Tb crystals.

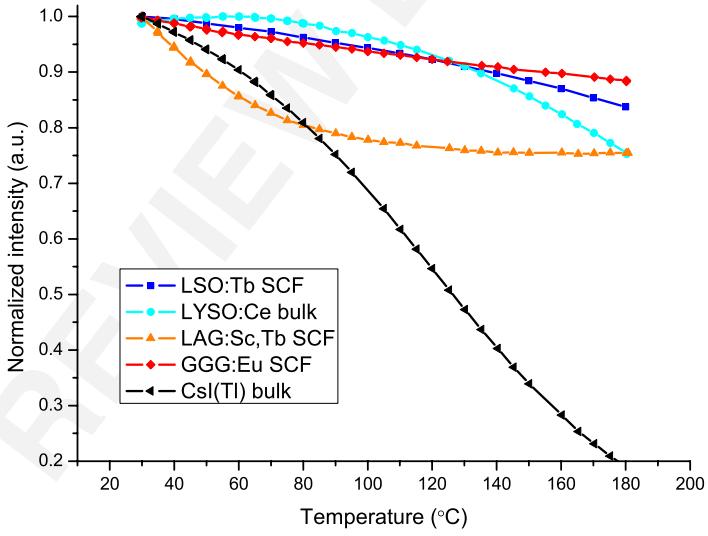

Fig. 9. Influence of the temperature between RT and 180^{o}C on the conversion efficiency of LSO:Tb SCF, LYSO:Ce bulk, LAG:Sc,Tb SCF, GGG:Eu SCF and CsI(Tl) bulk.

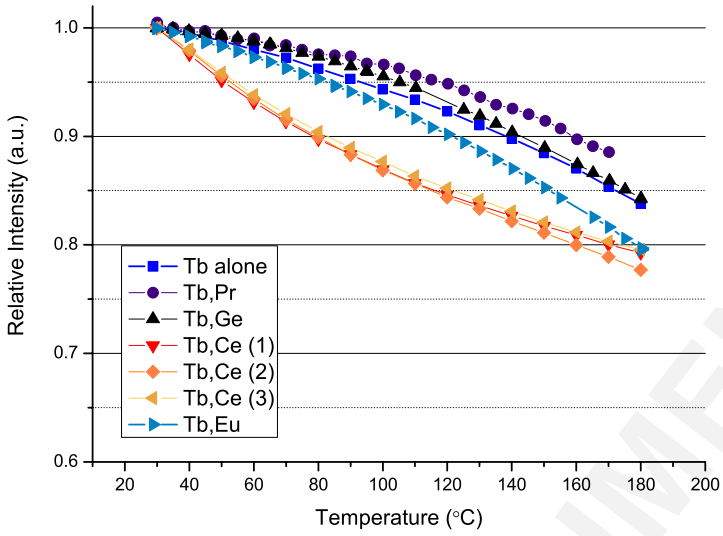

Fig. 10. Influence of the codopant on the conversion efficiency's response to temperature. Note the different decay shape when Ce^{3+} is used as a codopant. The three curves for LSO:Tb,Ce (1),(2) and (3) correspond to three different LSO:Tb thin films, all codoped with Ce^{3+}.

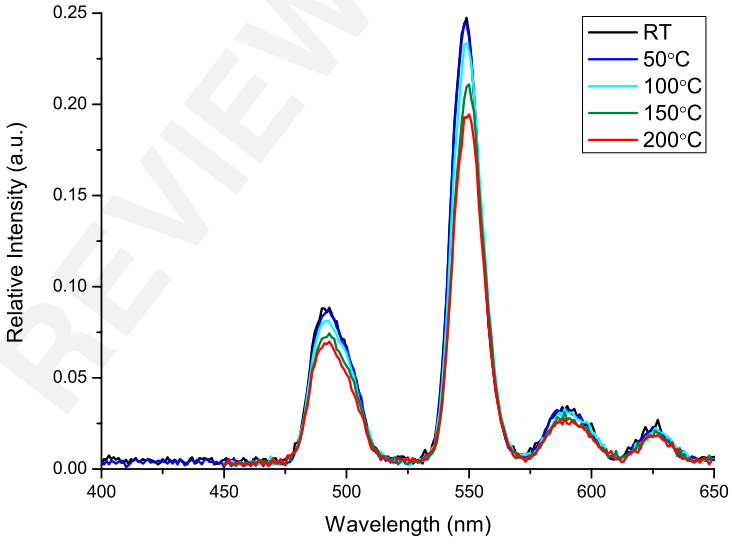

Fig. 11. Emission spectrum of LSO:Tb as a function of temperature (50^{o}C, 100^{o}C, 150^{o}C and 180^{o}C).

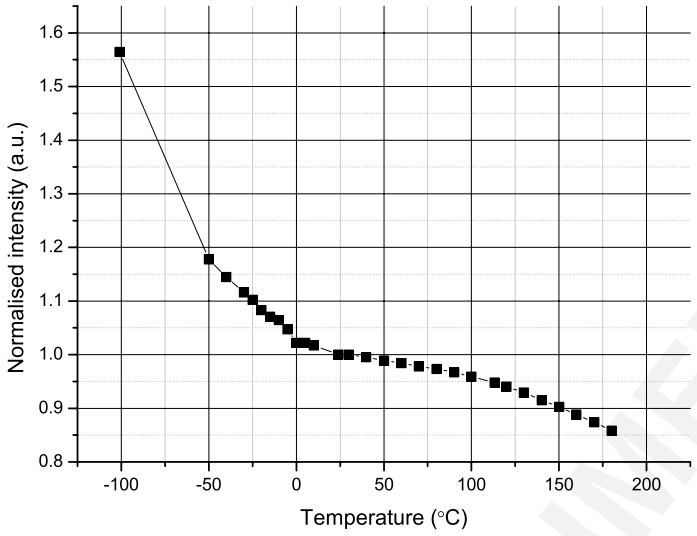

Fig. 12. LSO:Tb SCF conversion efficiency (normalised with respect to the conversion efficiency at RT), as a function of the temperature.

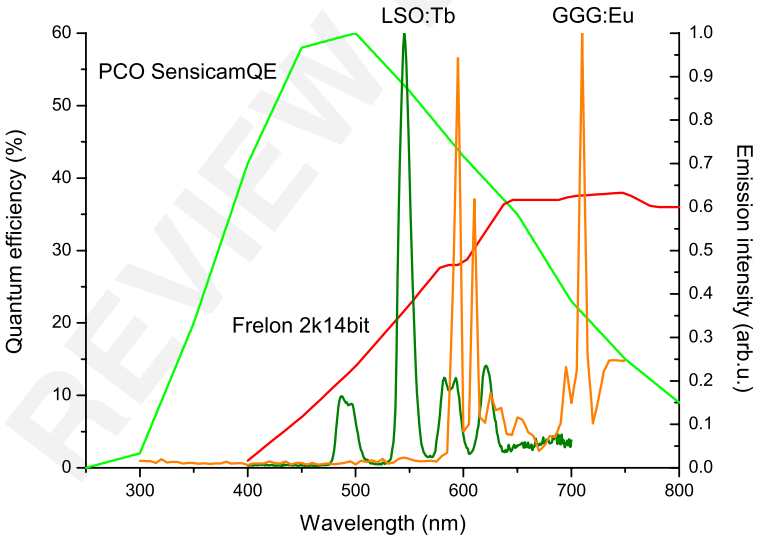

Fig. 13. Quantum efficiency of a PCO SensicamQE CCD camera (with interline transfer chip) and the FReLoN 2k (with front-illuminated e2v chip). The emission spectra of LSO:Tb (dark green) and GGG:Eu (orange) are displayed on the same plot to highlight the compatibility with both cameras, respectively.

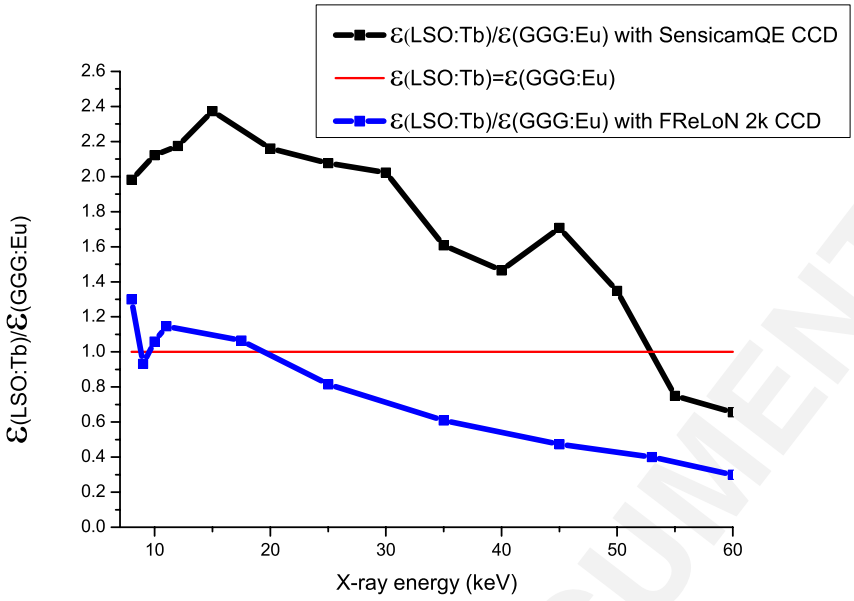

Fig. 14. Ratio of the efficiency obtained with a LSO:Tb SCF over the efficiency obtained with a GGG:Eu SCF, for two imaging systems based on different CCD cameras: a) FReLoN 2k (front-illuminated e2v chip), blue curve and b) PCO SensicamQE (interline transfer chip), black curve.

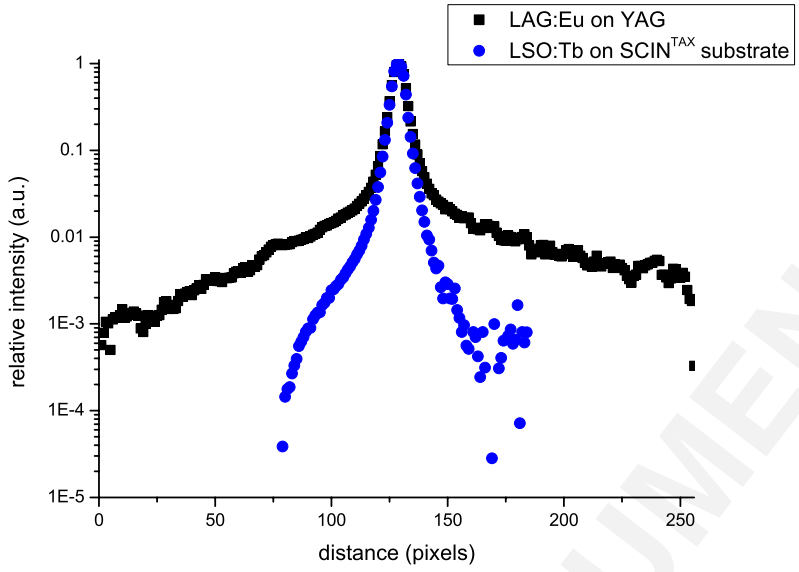

Fig. 16. Line Spread Function at 24 keV comparing the LSO:Tb SCF on its substrate and a LAG:Eu SCF grown on a YAG substrate. The LAG:Eu was used with a visible light filter to reduce the emission from the substrate. Note however the large tail of the LSF due to the remaining emission from the substrate.

Synopsis

The performance of a novel LSO-based thin film single crystal scintillator for synchrotron-based hard X-ray micro-imaging is characterised. An indirect X-ray imaging detector equipped with such a LSO screen shows improved detective quantum efficiency as well as higher spatial resolving power compared to common scintillator materials.